

Contents lists available at ScienceDirect

Mechanical Systems and Signal Processing

journal homepage: www.elsevier.com/locate/ymssp



A parameter identification method for continuous-time nonlinear systems and its realization on a Miura-origami structure



Zuolin Liu^a, Hongbin Fang^{a,b,*}, Kon-Well Wang^b, Jian Xu^a

^a School of Aerospace Engineering and Applied Mechanics, Tongii University, Shanghai 200092, China

ARTICLE INFO

Article history: Received 20 November 2017 Received in revised form 8 February 2018 Accepted 13 February 2018

Keywords:
Galerkin finite element
B-splines
Origami structures
Bistable systems
Nonlinear systems

ABSTRACT

Many mechanical systems are nonlinear and often high-dimensional, Constructing accurate models for continuous-time nonlinear systems calls for effectively identifying their parameters, whereas measurement noise and sensitivity to initial conditions make the identification challenging. This paper proposes a new parameter identification method for ordinary differential equations based on the idea of B-Spline Galerkin finite element. In this approach, the system's solution is globally constructed by a set of B-Splines. With Galerkin weak formulation, instead of taking analytical derivatives on basis functions, the differential terms are eliminated through integration by parts so that the measurement noise will not be amplified. Then least square algorithms can be adopted for solving the optimization problem to estimate the parameters. By solving two intractable testbed problems, the coupled Chua's circuits and the Tank reactor equations, we show that the new approach is effective and efficient in dealing with systems with highdimensionality, complex nonlinearity, discontinuous input and output, and noisy data without specific pre-processing. In addition, this method is employed to identify the geometrical and mechanical parameters of a Miura-origami structure under base excitation. which possesses complex global nonlinearity, exhibits chaotic responses, and suffers from significant measurement noise. The proposed method gains success in dealing with this system; based on the identified parameters, the corresponding constituent forcedisplacement relation and the simulation results agree well with the experiments.

© 2018 Elsevier Ltd. All rights reserved.

1. Introduction

Ordinary differential equations (ODEs) arise in many contexts of natural and social science for describing the temporal evolution of anything from a rocket launching to the spread of a disease, from electrical circuits to economic development [1]. Under some circumstances, the models are based on well-established physical principles, the parameters of ODEs can be determined from first principles or direct measurement. On the other hand, many ODEs are mathematical simplifications of actual systems or even data-driven models [2], their parameters cannot be determined through either of these approaches, which as a result, calls for parameter identification from experimentally measured data.

^b Department of Mechanical Engineering, University of Michigan, Ann Arbor, MI 48109, USA

^{*} Corresponding author at: School of Aerospace Engineering and Applied Mechanics, Tongji University, Shanghai 200092, China. *E-mail address:* fanghongbin@tongji.asia (H. Fang).

The nonlinear least square (NLS) method is a straightforward approach for parameter estimation in ODEs [3,4]. Usually, closed-form solutions do not exist for a generic nonlinear ODE model. Hence, numerical integration scheme such as the Runge-Kutta algorithm is often used to obtain approximate solutions of the ODEs for a given set of parameters and initial conditions; then an iterative procedure is applied to find the optimal estimation of the unknown parameters that minimize the residual sum of squares of the differences between the experimental data and the numerical solutions [5]. Note that the system's initial conditions are always difficult to know accurately or are with noise. To solve this issue, one solution is to treat the initial conditions as an additional set of unknown parameters in the minimization scheme [6,7]. However, the NLS method calls for numerical integration during each iteration, which therefore induces problems including high computational costs and slow convergence, especially for those systems in high dimension and with complex nonlinearities.

An alternative to iterative numerical integration is to build a regression model using measured discrete-time data and their higher-order derivatives in a "direct approach" [8–10]. Here the derivatives can be approximated through various discrete-time algebraic operators, such as bilinear transform, forward/backward/central difference, or generalized finite difference operators [9–11]. Then the least squares method would be desirable to apply because of its good numerical properties and low computational burden, especially for fast or non-uniform sampling. Particularly, recent research has demonstrated the advantages of difference operators (i.e., the delta 'ô' operator) because the identified model based on discrete-time representation has structural similarity to the continuous-time ODE-model, and the identified parameters approach to their continuous-time counterparts as the sampling interval tends to zero [10,12,13]. These estimation methods have been applied in both linear and nonlinear continuous-time system identification [10,12–15]. Note that in order to derive high-order derivative, repeated numerical differences on data are unavoidable in these approaches, which may cause noise amplification and a biased least squares estimate. To overcome this deficiency, various denoising algorithms [16–18] and bias-removal methods [12,14] have been proposed. However, for those systems that are extremely sensitive to parameters, such as chaotic systems [10,19], the denoising and bias-removal approaches would not be effective. To identify and correct the errors and biases, the system's underlying dynamic behavior needs to be exploited, which on the other hand, is always cumbersome and case-dependent.

Another way to avoid iterative numerical integration is to represent the solution globally via a set of convenient basis functions. Then the numerical difference used in the abovementioned discretization-based methods can be replaced by analytical derivatives of the basis functions. The choice of basis is crucially important for taking derivatives, because a very accurate representation of the data may exhibit high-frequency small-amplitude oscillations that are catastrophic for derivative estimation. Generally, Fourier basis [20,21] is always adopted for periodic data, and B-spline basis [22,23] or wavelets basis [24,25] for open-ended data. In addition to the type of basis, deciding the number of bases is also a dilemma: the more basis functions, the better fit to the data, but with the risk of simultaneously fitting the undesired noise and amplifying the noise when taking derivatives; while with fewer basis functions, important smooth characteristics that we are trying to achieve may be missed [26]. Certain techniques have been proposed to tackle this dilemma, such as stepwise variable selection and variable-pruning methods [27] for adding or dropping basis functions, iteratively correcting and fitting the measurement [22], and roughness penalty for avoiding over-fitting [26]. For example, with the roughness penalty approach, although the number of basis functions is equal or greater than that of the knots, penalties will be applied to the roughness so that the fitted curve would emphasize more on the smooth characteristics of the data. However, a new problem arises that how much degree of roughness penalty should be applied; determining of which can be achieved through, e.g., the generalized cross-validation method [28], but is always computationally intensive.

Note that none of the parameter identification methods would be effective in all scenarios. In practice, some essential issues need to be taken into account when proposing a new method. First, the method has to be computationally efficient that each trial can be completed in a short time. Second, the method should be robust under noise, since a noisy measurement is always unavoidable. Third, the method is expected to be able to deal with complex nonlinearity and high dimensionality. In this paper, inspired by the B-Spline Galerkin finite element method [29,30], a new identification approach is developed. More specifically, in this method, although still relying on basis functions (B-Spline) to globally represent the solution, derivatives on basis functions are replaced by analytical integration-by-parts based on the Galerkin weak formulation. Hence, this method not only removes the need for time-consuming numerical integrations but also avoids numerical differences on discrete data or derivatives on basis functions that may induce undesired noise amplification. Note that similar ideas based on conventional Galerkin finite element method [31] have been proposed in [32], where piecewise-liner basis functions were adopted for constructing the solutions of linear systems (truss structures). In this research, via solving two numerical testbed problems and dealing with a practical Miura-origami (Miura-ori) dynamic problem, we show that the new method extends its applicability to high-dimensional systems with complex nonlinearity, and is both efficient and robust. Therefore, the method developed in this paper significantly advances the state of the art in terms of broad applicability, computationally efficiency, and robustness.

The rest of the paper is organized as follows. Section 2 introduces the system we are to identify and three problems that will be tackled by the new method, including two numerical testbed problems and a Miura-ori structure with strong non-linearity. This is followed by detailed descriptions of the proposed method and the optimization procedures for linear and nonlinear systems in Section 3. The effectiveness of the method is verified in Section 4 on the two testbed problems. In Section 5, the method is applied to identify the geometric and physical parameters of a Miura-ori structure under dynamic excitations. Finally, summary and heuristic discussions are presented in Section 6.

2. Problem statement

2.1. Description of the system

The ordinary differential equations (ODEs), after certain normalizations, can be represented as

$$\dot{\mathbf{x}}(t) = \mathbf{f}(\mathbf{x}, \mathbf{u}, t | \boldsymbol{\theta}),\tag{1}$$

where \mathbf{x} is an s-dimensional vector of variables evolving with time; \mathbf{f} represents a vector field; \mathbf{u} is an r-dimensional vector of the input or control; and $\mathbf{\theta} = [\theta_1, \theta_2, \dots, \theta_p]^T$ denotes a p-dimensional vector of unknown constant parameters that need to be identified, with true values $\mathbf{\theta}_{true}$; $t \in [a,b]$ ($0 \le a < b < \infty$) denotes the time. Assuming that the input and output variables can be measured at time instants t_i , $i = 1, \dots, N$; the corresponding measurements are $\hat{\mathbf{u}}(t_i)$ and $\hat{\mathbf{x}}(t_i)$, which are subject to measurement errors $\mathbf{e}_u(t_i) = \mathbf{u}(t_i) - \hat{\mathbf{u}}(t_i)$ and $\mathbf{e}_x(t_i) = \mathbf{x}(t_i) - \hat{\mathbf{x}}(t_i)$, respectively. The goal of parameter identification is to estimate $\mathbf{\theta}$ with these measurements.

2.2. Two numerical testbed problems

Two numerical testbed problems are examined to verify the effectiveness of the proposed identification method. Here we briefly introduce the two problems, with a major focus on the intractable issues. The first is the coupled Chua's Circuits [33–35], which is a complicated high-dimensional dynamical system with rich nonlinear, initial-condition-sensitive, and parameter-sensitive dynamics (e.g., chaos). The second is the Tank reactor equations [36,37], which describe a common ideal reactor type in chemical engineering, the continuous flow stirred-tank reactor (CSTR). The input variables of the Tank reactor equations are step functions, which will induce discontinuities in the output derivatives that would severely complicate the parameter estimation.

2.2.1. Coupled Chua's circuits

Fig. 1(a) shows four Chua's circuits that are mutually coupled via six linear resistors R_c . The coupled Circuits' dynamics is described by the following state equations of dimension-12 [33]:

$$\begin{cases} \dot{v}_{C1j} = \frac{1}{C_{1j}} \left[\frac{1}{R_{j}} (v_{C2j} - v_{C1j}) - f(v_{C1j}) + \frac{1}{R_{C}} (-3v_{C1j} + \sum_{i}^{i \neq j} v_{C1i}) \right], \\ \dot{v}_{C2j} = \frac{1}{C_{2j}} \left[\frac{1}{R_{j}} (v_{C1j} - v_{C2j}) + i_{Lj} \right], \\ \dot{i}_{Lj} = -\frac{1}{I_{j}} [v_{C2j} - R_{0j} i_{Lj}], \end{cases}$$

$$(2)$$

where j = 1, 2, 3, 4; v_{C1j} and v_{C2j} denote the voltages across the capacitors C_{1j} and C_{2j} , respectively; i_{lj} denotes the current flowing through the inductors L_j . The Chua's diode N_{Rj} (a type of two-terminal, nonlinear active resistor) in each Chua's circuit exhibits the following voltage-current relation (Fig. 1(b))

$$f(v_{C1j}) = G_b v_{C1j} + \frac{1}{2} (G_a - G_b) \times [|v_{C1j} + 1| - |v_{C1j} - 1|]. \tag{3}$$

Here except the resistors R_j , the other parameters of the Chua's circuits are assumed to be identical such that $C_{1j} = C_1$, $C_{2j} = C_2$, $L_j = L$, and $R_{0j} = R_0$, and $N_{Rj} = N_R$. Hence, totally there are 11 parameters to be identified (G_a , G_b , C_1 , C_2 , L, R_0 , R_C , R_1 , R_2 , R_3 , R_4).

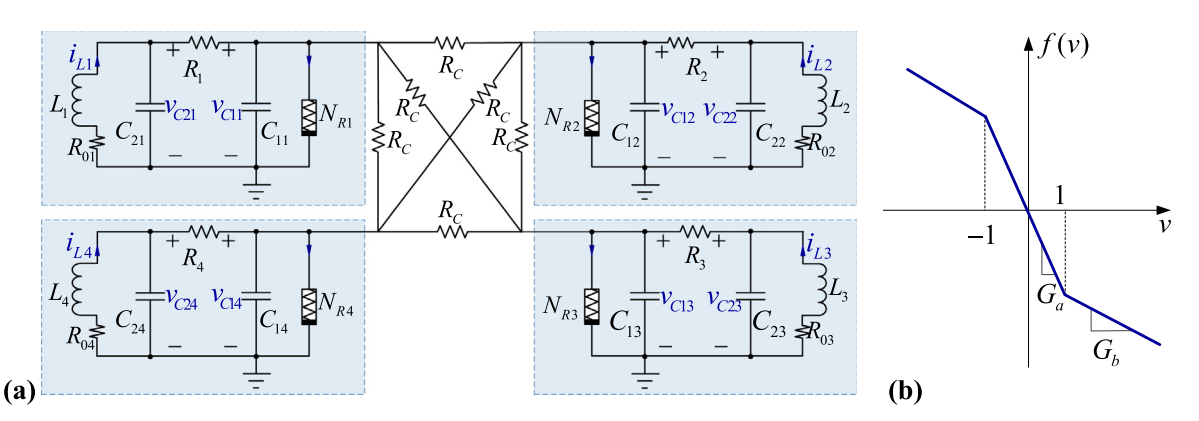


Fig. 1. (a) Diagram of the four mutually coupled Chua's circuits, where each Chua circuit is denoted by shaded rectangle. (b) Voltage-current characteristic of the Chua's diode N_{N} .

It has been numerically and experimentally evident that under critical parameters the mutually coupled Chua's Circuits would exhibit torus-doubling and even chaos phenomena [33], which are very sensitive to initial conditions and parameters. To identify the coupled circuits' parameters from noisy measurements, methods based on iterative numerical integration would be inappropriate because of the heavy computation burden caused by the system's high dimensionality, a large number of parameters, and dependence on initial conditions and parameters. The methods based on difference operators or basis functions would also become challenging because discrete difference on noisy data and derivations on basis functions would cause unacceptable noise amplification. Data pre-processing would be infeasible when the system is highly nonlinear, and especially when the responses are chaotic.

2.2.2. Tank reactor equations

The continuous flow stirred tank reactor (CSTR) is an ideal reactor type in chemical engineering that runs at steady state with continuous flows of reactants and products. Generally, the CSTR consists of an agitated-tank surrounded by a cooling jacket. The behavior of CSTR can be modeled by the following normalized equations (normalized by setting the volume of the tank to 1) [36,38,39]

$$\dot{C} = -\beta_{CC}(T, F_{in})C + F_{in}C_{in},
\dot{T} = -\beta_{TT}(F_{co}, F_{in})T + \beta_{TC}(T, F_{in})C + F_{in}T_{in} + \alpha(F_{co})T_{co},$$
(4)

where F_{in} , C_{in} and T_{in} are the flow rate, concentration, and temperature of the reagents, respectively; the reactor produces a product and leave the tank with concentration C and temperature T. F_{co} and T_{co} are the flow rate and temperature of the coolant in the cooling jacket, respectively. The weight functions β_{CC} , β_{TC} , β_{TT} and α depend on four parameters τ , κ , α and β , and can be expressed as:

$$\begin{split} \beta_{\text{CC}}(T,F_{in}) &= \kappa \exp\{-10^4 \tau (1/T - 1/T_{\text{ref}})\} + F_{in}, \\ \beta_{TT}(F_{co},F_{in}) &= \alpha(F_{co}) + F_{in}, \\ \beta_{TC}(T,F_{in}) &= 130 \beta_{\text{CC}}(T,F_{in}), \\ \alpha(F_{co}) &= \frac{aF_{co}^{1.5}}{F_{co} + aF_{co}^{0.5}/2}, \end{split}$$
 (5)

where T_{ref} is a fixed reference temperature, 350 K in this case. Here τ , κ , and a are the parameters to be identified; they determine the reaction kinetics and locate in the region [0.4, 1.8].

In this system, the state variables are controlled by five input variables F_{in} , F_{co} , C_{in} , T_{in} , and T_{co} . To examine its dynamics, square waves are always assigned to input parameters in virtual experiments. At critical parameters, the step changes of inputs will induce rapid variations of the outputs, which would generate discontinuities in the corresponding derivatives of the outputs. Hence, it would be challenging to find approximate basis functions to fit the responses; and traditional identification methods based on derivative estimations (i.e., numerical differences on discrete data or derivatives on basis functions) may become complicated.

2.3. Miura-ori structure

Origami is the art of paper folding and now refers the transformation of 2D flat sheets into sophisticated 3D shapes with diverse geometries. Origami-inspired structures and mechanical metamaterials have shown extraordinary properties and performances originating from the intricate geometries of folding, such as various deformation mechanisms [40], negative Poisson's ratio [40–42], self-locking [43,44], bistability and multistability [45–47], and tunable wave propagation [48,49], etc. These properties strongly depend on the geometric and physical parameters of origami, such as the folding dihedral angles and the crease rotational stiffness, which, unfortunately, are always difficult to know through simple measurement. Note that without accurate information on these parameters, getting reliable quantitative descriptions and predictions on origami structures' dynamics would be challenging. This issue arouses our interests on adopting dynamic identification methods to accurately estimate the parameters.

The origami structure to be studied in this paper is a stacked Miura-ori (SMO) structure, shown in Fig. 2(a). It is composed of two Miura-ori cells with different geometries, i.e., cell length parameters (a_x, b_x) and angle γ_x , where the subscript x takes 'A' or 'B' corresponding to cells A and B, respectively. To ensure compatibility between cells A and B when connecting them together, the geometric parameters have to satisfy the constraints $b_A = b_B = b$ and $\cos \gamma_B / \cos \gamma_A = a_A / a_B$. Folding of the SMO structure can be described through the folding angles θ_X or the dihedral angles between facets $\rho_{xi}(x=A,B,i=1,2,3,4)$. Note that folding of the SMO structure is one degree-of-freedom (say, with independent folding angle θ_A), then θ_B and all the other dihedral angles $(\rho_{xi}(x=A,B;i=1,2,3,4))$ and ρ_C can be determined (see Appendix A). The overall height of the SMO structure H can be expressed as

$$H = a_{\rm B} \sin \theta_{\rm B} \sin \gamma_{\rm B} - a_{\rm A} \sin \theta_{\rm A} \sin \gamma_{\rm A},\tag{6}$$

where $\theta_B = \arccos(\cos\theta_A \tan\gamma_A/\tan\gamma_B)$. Note that θ_A ranges between $-\pi/2$ and $\pi/2$, while θ_B keeps positive such that cell A bulges out of the larger cell B when $\theta_A < 0$ and nests into B otherwise. In what follows, for clarity, we denote the

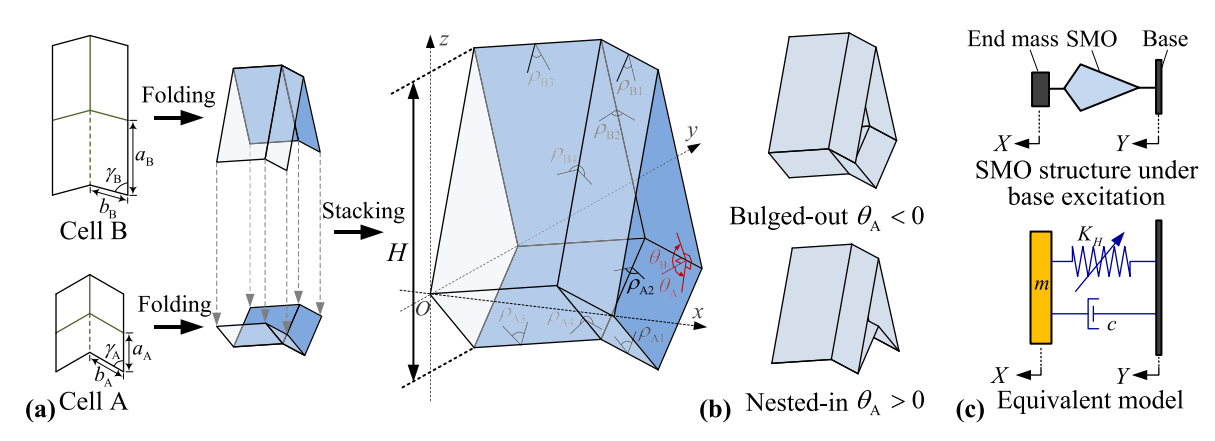


Fig. 2. (a) Construction and geometry of the SMO structure. (b) The bulged-out and nested-in configurations of the SMO structure. (c) The SMO structure under base excitation and its equivalent dynamic model.

configuration with $\theta_A < 0$ as 'bulged-out' and otherwise as 'nested-in' (Fig. 2(b)). On the other hand, Eq. (6) indicates that there is a one-to-one correspondence between H and θ_A . Then alternatively, the folding angle can be expressed by an implicit function of H, i.e., $\theta_A = \Theta(H)$.

Rotational stiffness is assigned to the creases in cell A, $K_{A1} = K_{A3} = k_Ab$, $K_{A2} = K_{A4} = k_Aa_A$; in cell B, $K_{B1} = K_{B3} = k_Bb$, $K_{B2} = K_{B4} = k_Ba_B$; and at the connecting creases, $K_C = k_Cb$. We assume that the torsional stiffness *per unit length* at cell A creases and connecting creases are the same and are relatively low, i.e., $k_A = k_C = k$, while the torsional stiffness per unit length at cell B creases is significantly higher than k (say, $k_B = \mu k$, $\mu > 1$ is a positive constant). Here the unit rotational stiffness k and the ratio μ are difficult to measure and need identification.

With the folding and dihedral angles as well as the torsional stiffness at the creases, the potential energy of the SMO structure $\Pi(\theta_A)$ can be obtained

$$\Pi(\theta_{A}) = \frac{1}{2} \left[\sum_{i=1}^{4} K_{Ai} (\rho_{Ai} - \rho_{Ai}^{0})^{2} + \sum_{i=1}^{4} K_{Bi} (\rho_{Bi} - \rho_{Bi}^{0})^{2} + 4K_{C} (\rho_{C} - \rho_{C}^{0})^{2} \right], \tag{7}$$

where ρ_{Ai}^{0} , ρ_{Bi}^{0} and ρ_{C}^{0} are the dihedral angles corresponding to the stress-free stable folding configuration ($\theta_{A} = \theta_{A}^{0}$) that no crease is deformed from its "natural" stress-free shape. The stress-free dihedral angle θ_{A}^{0} is difficult to be accurately measured and therefore also needs identification. The higher stiffness at the cell B creases as well as the non-unique angle relation between θ_{A} and θ_{B} are important for generating structural bistability. With appropriate values of μ , k, and θ_{A}^{0} , the potential energy would exhibit a double-well profile, indicating the existence of bistability [45,50]. Taking derivate of $\Pi(\theta_{A})$ with respect to H yields the force in the height direction F_{H}

$$F_H = \frac{\mathrm{d}\Pi}{\mathrm{d}\theta_A} \frac{\mathrm{d}H}{\mathrm{d}\theta_A},\tag{8}$$

which is also a function of θ_A . Hence, given a value of height H, the corresponding folding angle θ_A can be obtained from $\theta_A = \Theta(H)$; substituting it into F_H , the stiffness can be determined. It is worth pointing out here that F_H is a complicated nonlinear function of H, reflecting the strong global nonlinearity of the SMO structure.

If the bistable SMO structure is employed in a dynamic environment, one way to describe the system's response is to build an equivalent lumped-mass model in which the SMO structure is simplified into a massless nonlinear bistable spring (Fig. 2(c)). For example, if we apply a base excitation to the bistable SMO structure, its equation of motion can be expressed as

$$m\ddot{X}(t) + F_H(H(t)) + c(\dot{X}(t) - \dot{Y}(t)) = 0,$$
 (9)

where m is the equivalent lumped mass; Y(t) is the base displacement excitation, and X(t) is the displacement response of the lumped mass; c is the equivalent viscous damping coefficient, which is also unknown and needs to be identified.

In sum, in this bistable SMO structure under displacement excitation, there are four parameters to be identified: the unit torsional stiffness k, the stiffness ratio μ , the stress-free angle θ_A^0 , and the equivalent viscous damping coefficient c. Note that bistability is a strong nonlinear characteristic that would induce rich dynamics, including small-amplitude intra-well oscillations, large-amplitude inter-well steady-state and chaotic oscillations, etc. [50–54]. With the same excitation but different initial conditions, the structure would exhibit qualitatively different dynamics, either local responses that are confined to one of the potential well or global responses that surround or switch between two wells. Such initial-condition dependence would aggravate the computational burden of an identification method based on iterative numerical integration. On the other hand, the system possesses strong global nonlinearities and may exhibit global chaotic responses, and the dynamic

measurement would involve unavoidable noises, which also complicate the methods based on discrete differences or derivatives on basis functions.

3. System identification procedures

This section introduces the main procedures of the new identification method. Based on the Galerkin finite element approximation, first, a set of convenient basis functions $B_i(t) (i = 1, 2, ..., n)$ is employed to globally represent the input \mathbf{u} and the solution \mathbf{x} [1]

$$\mathbf{u} = \sum_{i=1}^{n} \mathbf{a}_i B_i(t), \tag{10}$$

$$\mathbf{x} = \sum_{i=1}^{n} \mathbf{b}_i B_i(t), \tag{11}$$

where \mathbf{a}_i and \mathbf{b}_i are the coefficient vectors. In this method, we use the same number of basis functions as the measured data $(t_i, \hat{\mathbf{u}}(t_i), \hat{\mathbf{x}}(t_i))$, $i = 1, \dots, N$ (n = N), so that in principle, any degree of variation in the data can be captured by the expansion. However, the large number of basis functions would lead to over-fitting of the data, i.e., the noise-induced variations are also fitted. This issue will be significantly magnified when derivatives are taken. Here new procedures are proposed to solve this problem, without imposing heavy calculation burden.

We construct a Galerkin weak formulation by multiplying both sides of Eq. (1) with basis function $B_i(t)$ and integrating both sides over the time interval [a, b],

$$\int_{a}^{b} B_{i}(t)\dot{\mathbf{x}}(t)dt = \int_{a}^{b} B_{i}(t)\mathbf{f}(\mathbf{x}, \mathbf{u}, t|\mathbf{\theta})dt. \tag{12}$$

The left-hand side of Eq. (12) can be rewritten based on the rule of integration by parts,

$$\int_{a}^{b} B_{i}(t)\dot{\mathbf{x}}(t)dt = B_{i}(t)\mathbf{x}(t)|_{a}^{b} - \int_{a}^{b} \dot{B}_{i}(t)\mathbf{x}(t)dt. \tag{13}$$

Assuming that the basis functions take zero at the boundary points a and b, Eq. (12) becomes

$$-\int_{a}^{b} \dot{B}_{i}(t)\mathbf{x}(t)dt = \int_{a}^{b} B_{i}(t)\mathbf{f}(\mathbf{x}, \mathbf{u}, t|\mathbf{\theta})dt. \tag{14}$$

Such procedures successfully avoid taking derivatives on the noisy data, thus solve the problem of noise amplification with high calculation efficiency.

A variety of basis functions are available for our method [26], in which the B-splines is considered as a convenient choice and has widely been used [55–57]. The B-splines of different orders can be recursively defined by

$$\varphi_{i}^{(0)}(t) = \begin{cases}
0, & t < t_{i}, \\
1, & t_{i} < t < t_{i+1}, \\
0, & t > t_{i},
\end{cases} (15)$$

$$\varphi_{i}^{(j)}(t) = \frac{t - t_{i}}{t_{i+1} - t_{i}} \varphi_{i}^{(j-1)}(t) + \frac{t_{j+i+1} - t}{t_{i+1} - t_{i+1}} \varphi_{i+1}^{(j-1)}(t).$$

In application, typically cubic B-splines are used (with j = 3); its explicit formula is given by

$$B_{i}(t) = \begin{cases} 0, & t \leqslant t_{i-2}, \\ \frac{1}{6h^{3}}(t - t_{i-2})^{3}, & t_{i-2} \leqslant t \leqslant t_{i-1}, \\ \frac{1}{6} + \frac{1}{2h}(t - t_{i-1}) + \frac{1}{2h^{2}}(t - t_{i-1})^{2} - \frac{1}{2h^{3}}(t - t_{i-1})^{3}, & t_{i-1} \leqslant t \leqslant t_{i}, \\ \frac{1}{6} + \frac{1}{2h}(t_{i+1} - t) + \frac{1}{2h^{2}}(t_{i+1} - t)^{2} - \frac{1}{2h^{3}}(t_{i+1} - t)^{3}, & t_{i} \leqslant t \leqslant t_{i+1}, \\ \frac{1}{6h^{3}}(t_{i+2} - t)^{3}, & t_{i+1} \leqslant t \leqslant t_{i+2}, \\ 0, & t \geqslant t_{i+2}, \end{cases}$$

$$(16)$$

where h is the spacing between the knots t_i (equally sampled). In this method, the sampling points are taken as the knots, which is a fixed setting once the measurement data have been obtained. With such procedure, the cumbersome knot-setting task is significantly simplified, and the noise amplification can be avoided by the proposed integration by parts. Fig. 3(a) shows five cubic B-splines with unit spacing length, and Fig. 3(b) displays the cubic B-spline and its first derivative (dashed line). It reveals that they are smooth, differentiable, and with compact-support, i.e., they take zero at the boundary points, satisfying the conditions for integration by parts.

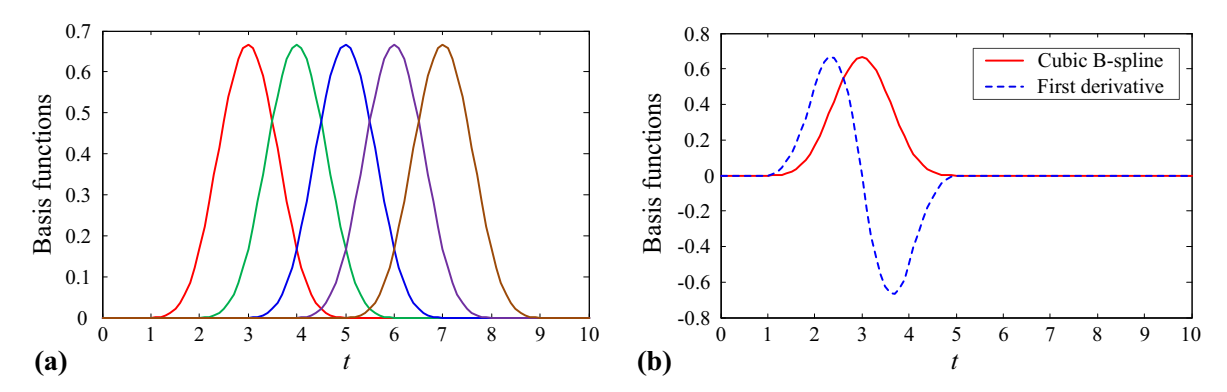


Fig. 3. (a) Five cubic B-splines with unit spacing length. (b) Cubic B-spline basis function and its first derivative.

Substituting the B-spline expression to Eq. (11), at knot t_i we have

$$\hat{\mathbf{x}}(t_i) = \sum_{i=1}^{n} \mathbf{b}_i B_i(t_i) = \mathbf{b}_{i-1} B_{i-1}(t_i) + \mathbf{b}_i B_i(t_i) + \mathbf{b}_{i+1} B_{i+1}(t_i) = \frac{1}{6} \mathbf{b}_{i-1} + \frac{2}{3} \mathbf{b}_i + \frac{1}{6} \mathbf{b}_{i+1}, \tag{17}$$

which can be written in matrix form as

$$\begin{pmatrix}
\hat{\mathbf{x}}(t_{-1}) \\
\hat{\mathbf{x}}(t_{0}) \\
\hat{\mathbf{x}}(t_{1}) \\
\vdots \\
\hat{\mathbf{x}}(t_{n}) \\
\hat{\mathbf{x}}(t_{n+1})
\end{pmatrix} = \frac{1}{6} \begin{pmatrix}
4 & 1 & 0 & \cdots & 0 \\
1 & 4 & 1 & \cdots & 0 \\
0 & 1 & 4 & \cdots & 0 \\
\vdots & & & & & \\
0 & \cdots & 1 & 4 & 1 \\
0 & \cdots & 0 & 1 & 4
\end{pmatrix} \begin{pmatrix}
\mathbf{b}_{-1} \\
\mathbf{b}_{0} \\
\mathbf{b}_{1} \\
\vdots \\
\mathbf{b}_{n} \\
\mathbf{b}_{n+1}
\end{pmatrix}.$$
(18)

Here $\hat{\mathbf{x}}(t_{-1})$ and $\hat{\mathbf{x}}(t_{n+1})$ are dummy values required for generating a determined system; they govern the behavior of \mathbf{x} at the boundaries and can be chosen such that the second derivatives at the boundaries are zero. The coefficient matrix in Eq. (18) is explicitly invertible, making it straightforward to solve the coefficient vectors $\mathbf{b}_i(i=-1,0,1,\ldots,n+1)$ and to obtain the corresponding interpolation function \mathbf{x} . Applying the same procedures on Eq. (10), the coefficient vectors $\mathbf{a}_i(i=-1,0,1,\ldots,n+1)$ and the interpolation function of input \mathbf{u} can be similarly obtained.

Due to the compact support property of the cubic B-splines (Eq. (16)), Eq. (14) becomes

$$-\int_{t_{i-2}}^{t_{i+2}} \dot{B}_i(t) \mathbf{x}(t) dt = \int_{t_{i-2}}^{t_{i+2}} B_i(t) \mathbf{f}(\mathbf{x}, \mathbf{u}, t | \mathbf{\theta}) dt.$$
 (19)

Based on Eq. (17), for the knots locating in time interval $[t_{i-2}, t_{i+2}]$, the interpolation function $\mathbf{x}(t)$ and $\mathbf{u}(t)$ can be simplified as

$$\mathbf{x}(t) = \sum_{k=i-3}^{i+3} \mathbf{b}_k B_k(t), \tag{20}$$

$$\mathbf{u}(t) = \sum_{k=i-3}^{i+3} \mathbf{a}_k B_k(t). \tag{21}$$

Substituting Eqs. (20) and (21) into Eq. (19), and letting

$$\mathbf{y}_{i} = -\int_{t_{i-2}}^{t_{i+2}} \dot{B}_{i}(t) \sum_{k=i-3}^{i+3} \mathbf{b}_{k} B_{k}(t) dt, \tag{22}$$

$$\mathbf{g}_{i}(\mathbf{\theta}) = \int_{t_{i-2}}^{t_{i+2}} B_{i}(t) \mathbf{f} \left(\sum_{k=i-3}^{i+3} \mathbf{b}_{k} B_{k}(t), \sum_{k=i-3}^{i+3} \mathbf{a}_{k} B_{k}(t), t \middle| \mathbf{\theta} \right) dt, \tag{23}$$

Eq. (19) becomes

$$\mathbf{y}_i = \mathbf{g}_i(\mathbf{\theta}). \tag{24}$$

Defining the loss function as

$$L(\boldsymbol{\theta}) = \sum_{i=3}^{N-3} (\mathbf{y}_i - \mathbf{g}_i(\boldsymbol{\theta}))^2, \tag{25}$$

then the unknown parameters can be estimated by minimizing $L(\theta)$. In what follows, cases with $\mathbf{f}(\mathbf{x}, \mathbf{u}, t|\theta)$ being linear or nonlinear in θ will be discussed, respectively.

3.1. Optimization with linear parameters

There are many models in physics, engineering, biology, and chemistry that are linear in their parameters. In these scenarios, Eq. (1) can be rewritten as

$$\dot{\mathbf{x}}(t) = \mathbf{f}(\mathbf{x}, \mathbf{u}, t | \mathbf{\theta}) = \mathbf{Z}(\mathbf{x}, \mathbf{u}, t) \cdot \mathbf{\theta}. \tag{26}$$

Then Eq. (23) can be transformed into

$$\mathbf{g}_{i}(\boldsymbol{\theta}) = \int_{t_{i-2}}^{t_{i+2}} B_{i}(t) \mathbf{Z} \left(\sum_{k=i-3}^{i+3} \mathbf{b}_{k} B_{k}(t), \sum_{k=i-3}^{i+3} \mathbf{a}_{k} B_{k}(t), t \right) dt \cdot \boldsymbol{\theta} = \mathbf{X}_{i} \cdot \boldsymbol{\theta}, \tag{27}$$

and Eq. (25) can be written as

$$L(\mathbf{\theta}) = \sum_{i=2}^{N-3} (\mathbf{y}_i - \mathbf{X}_i \cdot \mathbf{\theta})^2, \tag{28}$$

or in a matrix form

$$L(\boldsymbol{\theta}) = \sum_{i=2}^{N-3} (\mathbf{y}_i - \mathbf{X}_i \cdot \boldsymbol{\theta})^2 = \frac{1}{2} (\mathbf{Y}_{Lin} - \mathbf{X}_{Lin} \cdot \boldsymbol{\theta})^T (\mathbf{Y}_{Lin} - \mathbf{X}_{Lin} \cdot \boldsymbol{\theta}),$$
(29)

where the subscript "Lin" indicates the situation with linear parameters, and

$$\mathbf{X}_{Lin} = \left[\mathbf{X}_{3}^{T}, \mathbf{X}_{4}^{T}, \cdots, \mathbf{X}_{N-3}^{T}\right]^{T},\tag{30}$$

$$\mathbf{Y}_{lin} = [\mathbf{y}_3, \mathbf{y}_4, \cdots, \mathbf{y}_{N-3}]^T. \tag{31}$$

Eq. (29) suggests that the loss function is a quadratic form in the linear scenario, and the optimal parameters can be obtained by the one-shot Least Square algorithm. In detail, by taking derivate on Eq. (29) with respect to θ , we get

$$\frac{\partial L(\mathbf{\theta})}{\partial \mathbf{\theta}} = -\mathbf{X}_{Lin}^T \mathbf{Y}_{Lin} + \mathbf{X}_{Lin}^T \mathbf{X}_{Lin} \cdot \mathbf{\theta}. \tag{32}$$

Then the optimum estimation can be obtained by letting Eq. (32) equal zero, i.e.

$$\boldsymbol{\theta} = \left(\mathbf{X}_{Lin}^T \mathbf{X}_{Lin}\right)^{-1} \mathbf{X}_{Lin}^T \mathbf{Y}_{Lin}. \tag{33}$$

3.2. Optimization with nonlinear parameters

Here we discuss a more general case that the ODEs are nonlinear in terms of parameters. It is more complicated than the linear case since the one-shot Least Square algorithm cannot be applied directly; instead, iterative minimization routines are adopted in this study. In each iteration, we linearize the nonlinear equations through Taylor series expansion so that the one-shot algorithm can still be used on the obtained linear form.

Denoting the initial parameter guess as θ_0 and expanding the function $\mathbf{f}(\mathbf{x}, \mathbf{u}, t|\theta)$ into linear form in the neighborhood of θ_0 , we get

$$\mathbf{f}(\mathbf{x}, \mathbf{u}, t | \mathbf{\theta}) = \mathbf{f}(\mathbf{x}, \mathbf{u}, t | \mathbf{\theta}_0) + \frac{\partial \mathbf{f}(\mathbf{x}, \mathbf{u}, t | \mathbf{\theta}_0)}{\partial \mathbf{\theta}} \delta \mathbf{\theta} + O((\delta \mathbf{\theta})^2), \tag{34}$$

where

$$\delta \theta = \theta - \theta_0. \tag{35}$$

Substituting Eq. (34) into Eq. (23) yields

$$\mathbf{g}_{i}(\mathbf{\theta}) = \mathbf{p}_{i}(\mathbf{\theta}_{0}) + \mathbf{q}_{i}(\mathbf{\theta}_{0})\delta\mathbf{\theta},\tag{36}$$

where

$$\mathbf{p}_{i}(\mathbf{\theta}_{0}) = \int_{t_{i-2}}^{t_{i+2}} B_{i}(t) \mathbf{f} \left(\sum_{k=i-3}^{i+3} \mathbf{b}_{k} B_{k}(t), \sum_{k=i-3}^{i+3} \mathbf{a}_{k} B_{k}(t), t \middle| \mathbf{\theta}_{0} \right) dt, \tag{37}$$

$$\mathbf{q}_{i}(\mathbf{\theta}_{0}) = \int_{t_{i-2}}^{t_{i+2}} B_{i}(t) \frac{\partial \mathbf{f}\left(\sum_{k=i-3}^{i+3} \mathbf{b}_{k} B_{k}(t), \sum_{k=i-3}^{i+3} \mathbf{a}_{k} B_{k}(t), t \middle| \mathbf{\theta}_{0}\right)}{\partial \mathbf{\theta}} dt. \tag{38}$$

Thus the loss function can be rewritten as

$$L(\mathbf{\theta}) = \sum_{i=3}^{N-3} (\mathbf{y}_i - \mathbf{p}_i(\mathbf{\theta}_0) - \mathbf{q}_i(\mathbf{\theta}_0)\delta\mathbf{\theta})^2, \tag{39}$$

or in a matrix form

$$L(\mathbf{\theta}) = \frac{1}{2} (\mathbf{Y}_{Non} - \mathbf{X}_{Non} \cdot \delta \mathbf{\theta})^{T} (\mathbf{Y}_{Non} - \mathbf{X}_{Non} \cdot \delta \mathbf{\theta}), \tag{40}$$

where the subscript "Non" denotes the situation with nonlinear parameters and

$$\mathbf{X}_{Non} = \left[\mathbf{q}_3^T(\boldsymbol{\theta}_0), \mathbf{q}_4^T(\boldsymbol{\theta}_0), \dots, \mathbf{q}_{N-3}^T(\boldsymbol{\theta}_0)\right]^T. \tag{41}$$

$$\mathbf{Y}_{Non} = [\mathbf{y}_{3} - \mathbf{p}_{3}(\mathbf{\theta}_{0}), \mathbf{y}_{4} - \mathbf{p}_{4}(\mathbf{\theta}_{0}), \dots, \mathbf{y}_{N-3} - \mathbf{p}_{N-3}(\mathbf{\theta}_{0})]^{T}. \tag{42}$$

Similarly, taking derivate on Eq. (40) with respect to $\delta\theta$ and letting it be zero, we get

$$\delta \mathbf{\theta} = (\mathbf{X}_{\text{Non}}^T \mathbf{X}_{\text{Non}})^{-1} \mathbf{X}_{\text{Non}}^T \mathbf{Y}_{\text{Non}}. \tag{43}$$

Substituting Eq. (43) into Eq. (35) again and replacing θ_0 , we obtain an updated θ_0 , i.e.,

$$\theta_0 \to \delta \theta + \theta_0$$
. (44)

Repeating this calculating-updating procedure until $\delta\theta$ reduces to an acceptable tolerance, the unknown parameters will converge to their true values.

4. Simulation studies

This section discusses the numerical studies on the Chua's Circuit and the Tank reactor, introduced in Section 2, to verify the effectiveness of the new identification procedures proposed in the previous section.

4.1. Parameter identification for the coupled Chua's circuit

The coupled Chua's circuit shown in Fig. 1 is a 12-dimensional nonlinear system (Eq. (12)). There are 11 parameters to be identified. Their critical values are set as $G_a = -0.74$, $G_b = -0.41$, $C_1 = 0.01$, $C_2 = 0.1$, L = -0.01868, $R_0 = 0.019$, $R_C = 10$, $R_1 = 1.599$, $R_2 = 1.228$, $R_3 = 0.917$, $R_4 = 3.628$ such that torus-doubling phenomenon can be generated [24]. The initial conditions for all 12 state variables are random numbers between 0 and 1. We sample the simulation data between 0 and 150 with spacing 0.02 and corrupt the sampling data by Gaussian white noise with a 30 dB signal-to-noise ratio (SNR).

In the identification process, the initial parameters are assumed to be 50% deviated from the true values, and the cutoff error is $\varepsilon=10^{-5}$. With the proposed procedures, the value of each parameter in each iteration step is shown in Fig. 4(a)–(c), where the dotted lines denote the true values we set in the simulation. It reveals that all parameters converge to their true values quickly. This is demonstrated by Fig. 4(d) that the iteration converges exponentially in the neighborhood of the true value θ_{true} ; after seven iterations, the step length has dropped below the cutoff error, stopping the iteration. The overall identification results are summarized in Table 1; for the 11 parameters, the relative errors between the identified values and the true values are lower than 0.04%, demonstrating the effectiveness and accuracy of the proposed method.

To further investigate the robustness of the identification method with respect to noise, additional simulations with different noise level have been carried out. Specifically, the simulated signals are corrupted by Gaussian white noise with SNR varying from 90 dB to 10 dB. Fig. 4(e) displays the noisy signals with SNR = 70 dB, 30 dB, and 10 dB. To compare the robustness of the identification, the overall error is defined as $\delta = \text{norm}(\theta_{id} - \theta_{true})/\text{norm}(\theta_{true})$, where θ_{id} is the vector of the identified values, and θ_{true} is the vector of the true parameter values. Fig. 4(f) shows the overall error with respect to different noise levels. With relatively small noise (SNR \geq 30 dB), the identified values agree well with the true values, showing very low errors. With the decrease of SNR, i.e., with the increase of noise level, the corresponding overall error grows rapidly. Especially, the error becomes significant when SNR approaches 10 dB (i.e., the noise is as strong as the signal in terms of root-mean-square (RMS) amplitude). Overall, our method shows acceptable robustness with respect to noises. For example, when SNR = 20 dB, i.e., the noise RMS amplitude reaches 10% of the signal RMS amplitude, the overall error is still less than

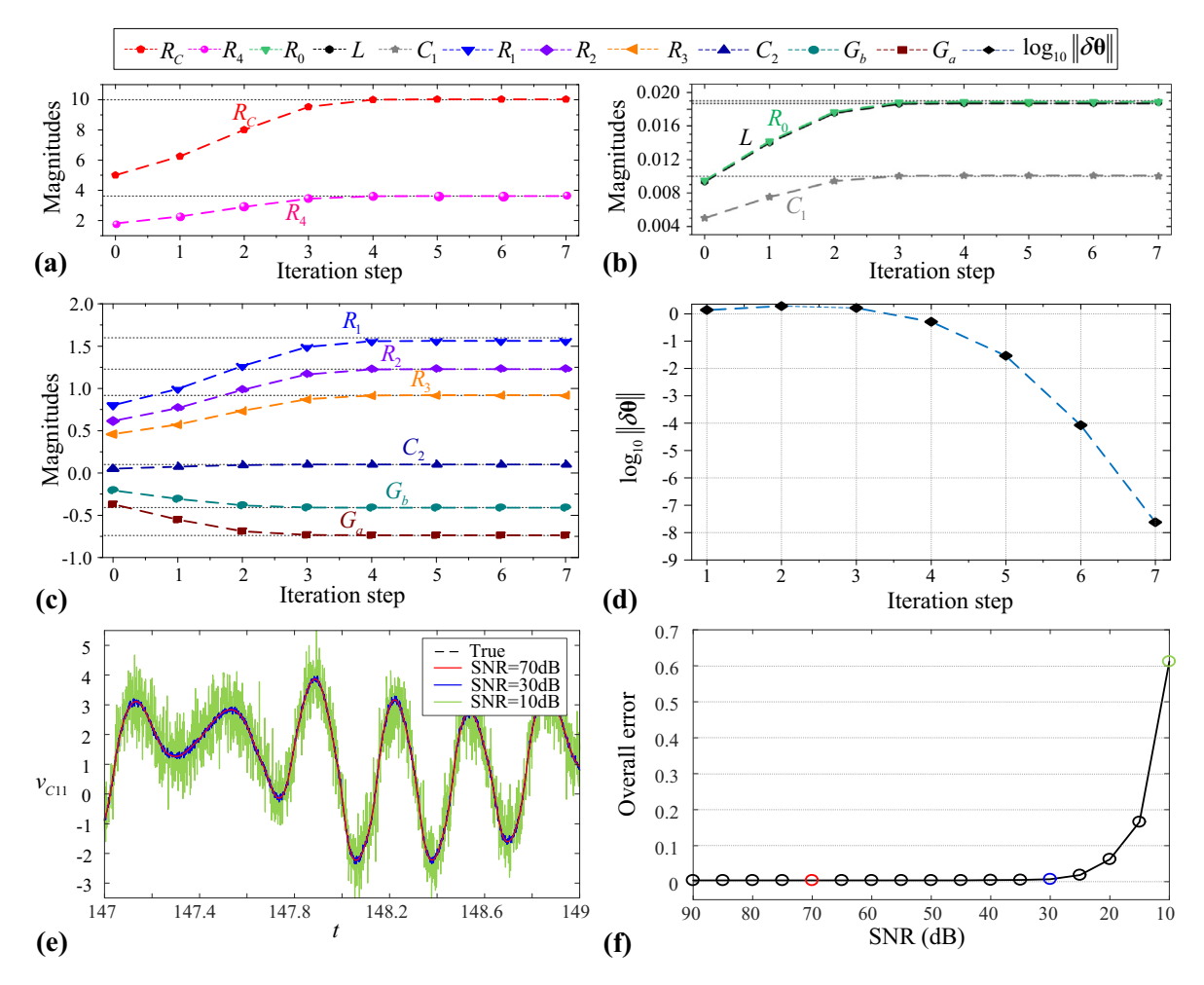


Fig. 4. Parameter identification of the coupled Chua's circuit. (a)–(c) The convergence processes of the 10 identified parameters, where the true values are denoted by horizontal dotted lines; (d) the logarithm of $\delta\theta$ in each iteration step; (e) signals of ν_{C11} corrupted by noises with SNR = 70 dB, 30 dB, and 10 dB; and (f) the overall errors of the identification results with respect to different levels of noise.

Table 1 Identification results of the coupled Chua's circuit (with SNR = 30 dB).

Parameters	G_a	G_b	C ₁	C_2	L	R_0	R_C	R_1	R_2	R_3	R_4
Initial values	-0.3700	-0.2050	0.0050	0.0500	0.00934	0.0095	5.000	0.7995	0.6140	0.4585	1.8140
Identified values	-0.7397	-0.4101	0.0100	0.1000	0.01870	0.0190	9.998	1.5590	1.2280	0.9170	3.6287
True values	-0.7400	-0.4100	0.0100	0.1000	0.01868	0.0190	10.000	1.5990	1.2280	0.9170	3.6280
Relative errors	0.04%	0.02%	0.00%	0.00%	0.02%	0.00%	0.02%	0.00%	0.00%	0.00%	0.02%

10%. However, note that if the noise is significant enough to qualitatively change the signal (e.g., SNR = 10 dB, the signal is severely corrupted, see Fig. 4(e)), our method will lose its effectiveness.

4.2. Parameter identification for Tank reactor equations

The Tank reactor equations (Eqs. (4) and (5)) are also nonlinear in parameters. In this simulation, the parameters are chosen as $\tau = 0.8330$, $\kappa = 0.4610$, a = 1.6780 [25]. The five inputs are piecewise step functions shown in Fig. 5(a). We add 40 dB zero-mean Gaussian white noises to the outputs C(t) and T(t), shown in Fig. 5(b). In this system, three parameters, τ , κ , and a, need to be identified. Similarly, their initial values are set to be 20% deviated from the true values, and the cutoff error is $\varepsilon = 10^{-5}$.

Fig. 5(c) displays the magnitudes of these parameters in each iteration step. It reveals that with the proposed identification method, the parameters converge to the true values within 8 steps, with $\delta\theta$ exponentially decreasing to lower than 10^{-6} at the 8th step (Fig. 5(d)). The identification results are summarized in Table 2.

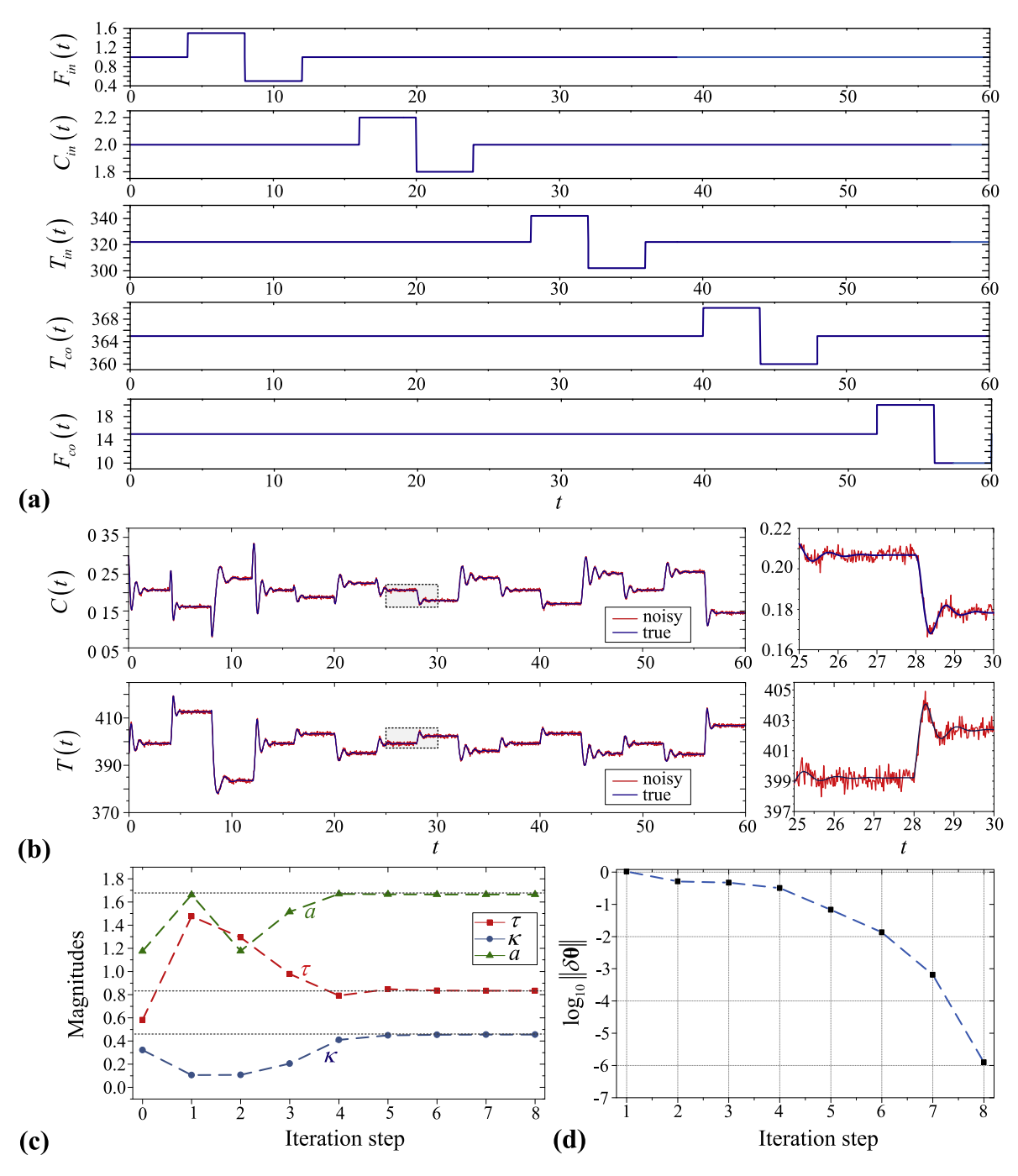


Fig. 5. Parameter identification of the Tank reactor equations. (a) The five piecewise inputs; (b) the two noisy outputs; (c) convergence processes of the identified parameters; and (d) the logarithm of $\delta\theta$ in each iteration step.

Table 2 Identification results of the Tank reactor equations.

Parameters	τ	κ	а
Initial values	0.6651	0.3694	1,3343
True values	0.8330	0.4610	1.6780
Identified values	0.8314	0.4617	1.6679
Relative errors	0.19%	0.15%	0.60%

Here we note that by numerically solving the two intractable testbed problems, i.e., the coupled Chua's circuit and the Tank reactor equations, advantages of the new identification method are revealed. First, the proposed approach does not call for time-consuming numerical integrations, therefore applicable to systems with high dimensionality and complex nonlinearity. Second, the method does not require numerical differences on measured data or analytical derivatives on basis functions, thus works well with noisy data. Third, the method is numerically efficient; it costs less than 1 min to get reliable estimations of the two testbed problems. These fully illustrate the great potential of the proposed method in solving various identification problems.

5. Parameter identification of a stacked Miura-ori structure

In addition to the numerical examples, this section investigates the dynamics of a stacked Miura-ori structure (SMO) to demonstrate the virtue of the proposed method. Here we first briefly introduce the prototyping, experimental setup, and the test procedures (see details in [50]), and then present the identification results.

5.1. Prototyping and experiments

The SMO prototype's geometric and mechanical parameters are listed in Table 3. The fabrication of an SMO prototype is shown in Fig. 6(a), where the origami facets are waterjet cut individually from 0.25-mm-thick stainless steel sheets; they are fixed to a 0.13-mm-thick adhesive-back plastic film (ultrahigh molecular weight (UHMW) polyethylene) to form two Miura-ori sheets. We paste 0.01-mm-thick pre-bent spring-steel stripes at the creases of the top sheet to provide strong torsional stiffness. The two sheets are stacked together into an SMO prototype. The obtained SMO prototype maintains rigid foldability because the steel facets are much stiffer than the creases; meanwhile, the stiffness at the creases with spring-steels is significantly higher than the stiffness of other creases, generating structural bistability. To facilitate installation of the prototype on the shaker, 3D-printed connectors are used (Fig. 6(b)). Note that here the bending stiffness of the plastic film (k), the bending stiffness of the spring-steel stripes (μk), and the pre-bent angle (θA) are all unknown.

Fig. 6(c) shows the experimental setup for the dynamic test. With the 3D-printed connectors, we are able to connect the SMO prototype onto the shaker and connect a lumped mass with the SMO prototype. Very light strings are used to suspend the SMO prototype. Harmonic base excitations $Y(t) = Y_0 \sin(\omega t)$ are applied to the SMO prototype in the horizontal direction (i.e., the height direction of the SMO structure), with frequency ω and amplitude Y_0 . During measurement, external perturbations are applied to the lumped mass to change the initial conditions so as to capture all possible dynamics. We use two laser vibrometers to synchronously measure the absolute steady-state motions (including the displacement and velocity) of the shaker $(Y(t), \dot{Y}(t))$ and the lumped mass $(X(t), \dot{X}(t))$. The excitation parameters are listed in Table 3.

Note that the stiffness changes with respect to the height of the SMO structure, i.e., K_H is a function of H(t). However, in the experiment, the height changes cannot be directly measured, rather, only X(t) and Y(t) are recorded. Hence, it is important to establish the relation between the measured X(t), Y(t) and the unmeasurable H(t). In measurement, there is a constant relation between them

$$X(t) + X_0 = Y(t) + H(t),$$
 (45)

where X_0 is a constant for determining the origin of X(t) measurement. Theoretically, X_0 equals to the height of the SMO structure at one stable configuration; while in each measurement, X_0 cannot be known accurately, because the measurement origin for each test cannot be set to be exactly identical, and there is unavoidable signal zero-drift. To address this issue, we treat X_0 as another parameter to be identified. Thus the equation of motion can be rewritten as

$$m(\dot{X}) + c(\dot{X} - \dot{Y}) + F_H(X - Y + X_0) = 0, \tag{46}$$

or in a standard state-space ODEs form

$$\dot{X} = V,
\dot{V} = -\frac{c}{m}(V - W) - \frac{1}{m}F_H(X - Y + X_0),$$
(47)

Table 3Parameters of the prototype and the excitation.

Parameter type	Parameters	Values	Parameter type	Parameters	Values
Geometry parameters	$b_A = b_B = b$ a_A	38.1 mm 38.1 mm	Mechanical parameters	$egin{aligned} k_A &= k_C \ k_B \ m \end{aligned}$	k μk 0.135 kg
	γ_A γ_B	60° 75°	Excitation parameters	ω Y_0	2-12 Hz Average: 6.17 mm Standard deviation: 0.397 mm

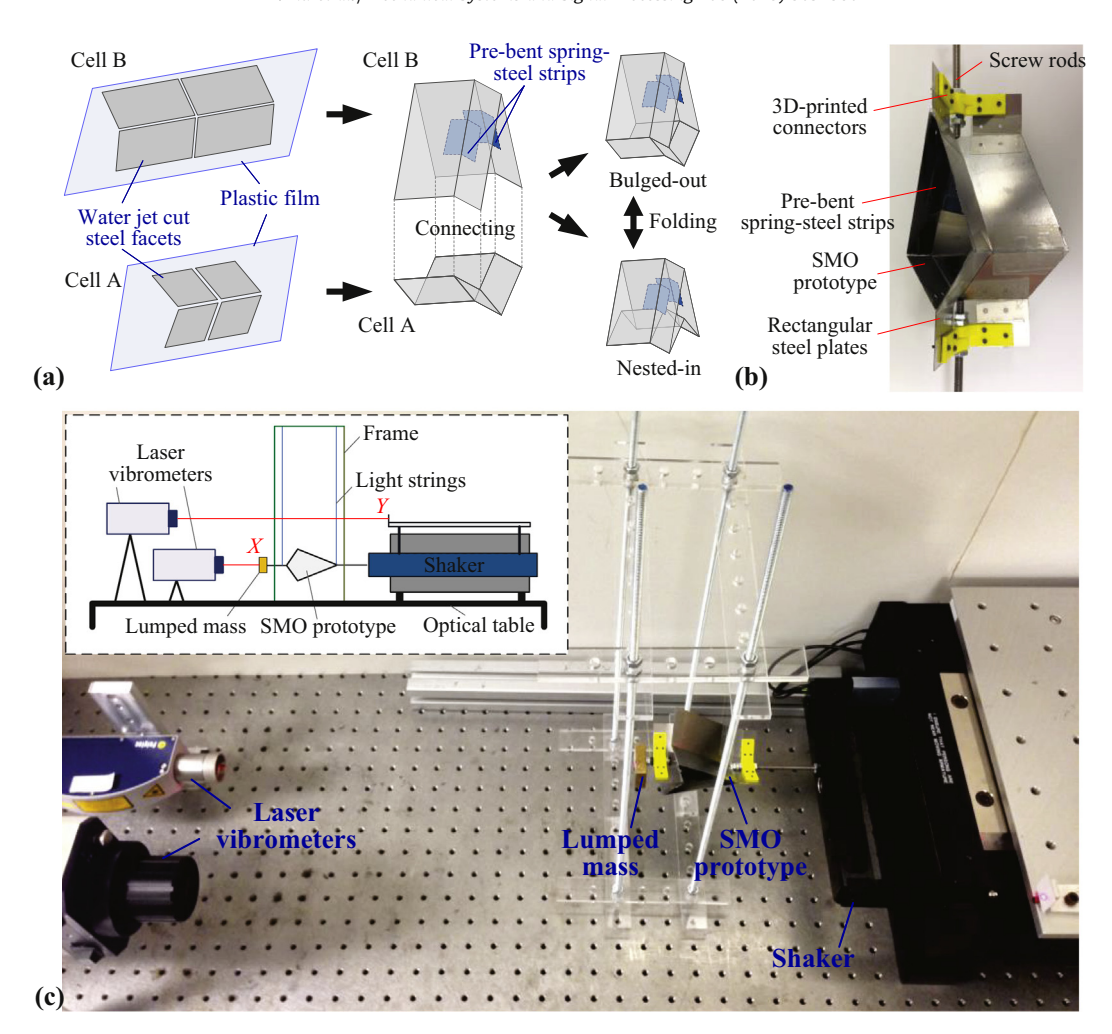


Fig. 6. Experimental prototype fabrication and test setup: (a) Schematic illustration of the prototyping procedures; (b) photo of the SMO prototype; and (c) sketch and photo of the test setup.

where $W = \dot{Y}$ is the velocity of the base excitation. Thus there are five parameters in total to be identified in this system, they are the unit torsional stiffness k, the stiffness ratio μ , the stress-free angle θ_A^0 , the equivalent viscous damping coefficient c, and X_0 . Here, except the damping coefficient c, the system is nonlinear in other parameters. The equivalent mass m is treated as measurable and is set as the total mass of the prototype, which does not affect the prediction of dynamics based on the identified parameters.

With the standard form, we can then apply the proposed method to identify the parameters. Considering that the bistable SMO structure can exhibit both small-amplitude intra-well responses (within one of the potential well) and large-amplitude inter-well responses (around or advantages of the new approach, we pick a large-amplitude inter-well chaotic response at excitation frequency 6.6 Hz for identification. Fig. 7 shows the measured time-histories of the state variables $\dot{X}(t)$, $\dot{Y}(t)$, and (X(t)-Y(t)), which are used in the identification process. Through fast Fourier transformation, their spectrograms are also given in Fig. 7(d). The chaotic nature of the response signals $(\dot{Y}(t)$ and (X(t)-Y(t))) can be observed from the continuous spectrum over a limited range, indicating the spread of energy over a wide bandwidth.

Note that F_H is an explicit function of θ_A given in Eq. (8), and the relationship between X_0 and θ_A can be derived by substituting Eq. (45) into Eq. (6)

$$X(t) - Y(t) + X_0 = a_B \sin \theta_B \sin \gamma_B - a_A \sin \theta_A \sin \gamma_A. \tag{48}$$

Thus, F_H is also an implicit nonlinear function of X_0 . In addition, since the stiffness of the film k may be very small, while the stiffness ratio μ can be very significant, hence rather than directly identifying k and μ , $k_1 = k$ and $k_2 = \mu k$ will be examined to prevent possible singularity and to accelerate the convergence. Applying the linearization process given in Eq. (34), we have

$$\frac{\partial \mathbf{f}(\mathbf{x}, \mathbf{u}, t | \boldsymbol{\theta}_0)}{\partial \boldsymbol{\theta}} = \begin{bmatrix} \frac{\partial \mathbf{f}}{\partial k_1} & \frac{\partial \mathbf{f}}{\partial k_2} & \frac{\partial \mathbf{f}}{\partial c} & \frac{\partial \mathbf{f}}{\partial \theta_A} & \frac{\partial \mathbf{f}}{\partial \theta_A} & \frac{\partial \boldsymbol{\theta}_A}{\partial X_0} \end{bmatrix}. \tag{49}$$

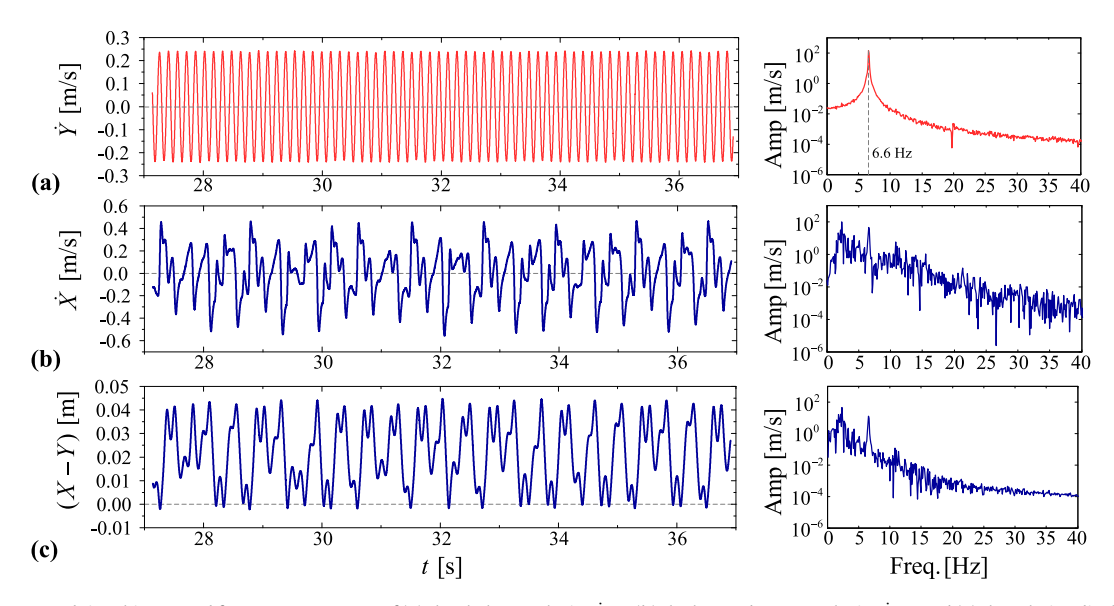


Fig. 7. Measured time history and frequency spectrum of (a) the shaker's velocity $\dot{Y}(t)$, (b) the lumped mass's velocity $\dot{X}(t)$, and (c) the relative displacement (X-Y) at the excitation frequency 6.6 Hz. Continuous frequency bands are observed in the responses' frequency spectrum, indicating their chaotic characteristics.

where **f** is the right-hand side terms of Eq. (47). The initial parameters are set as $k_1 = 0$, $k_2 = 5$, $\theta_A^0 = -\pi/3$, c = 1, and $X_0 = 0.051$, and the cut-off error is 10^{-3} . Then the other identification procedures can be successively applied. The identification algorithm converges after 19 iterations, with the step length lower than the cut-off error. The value of each parameter

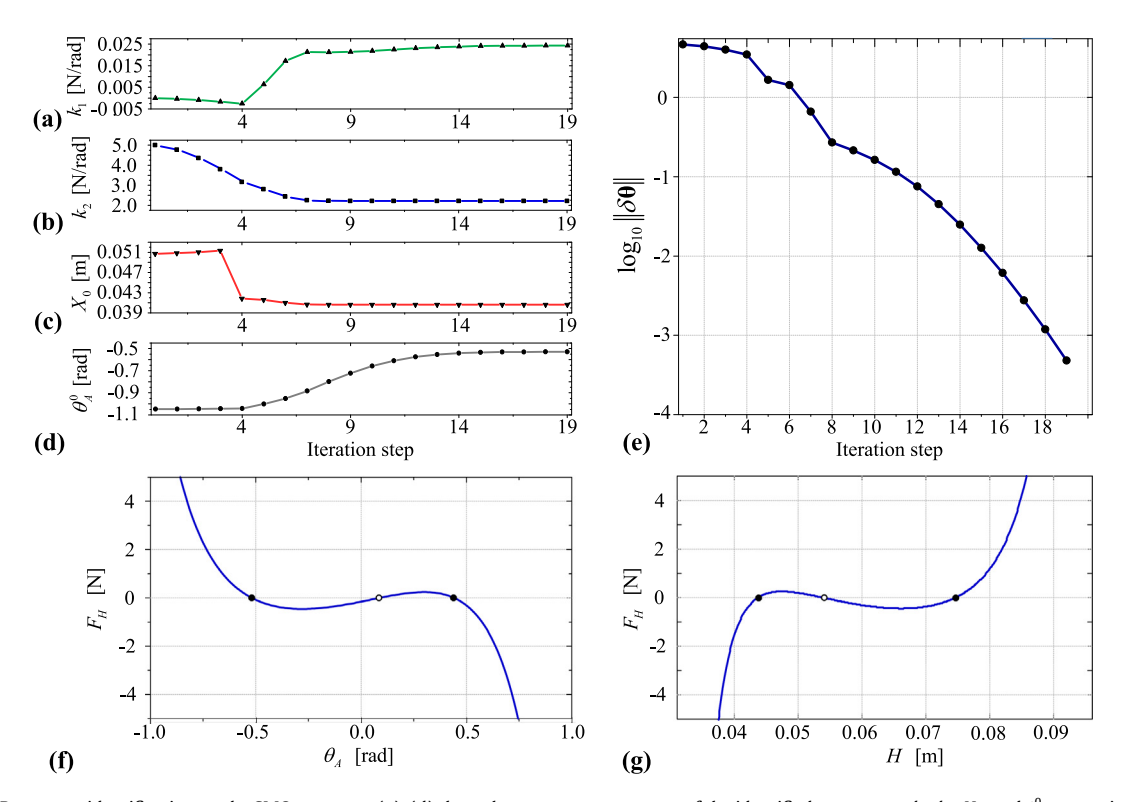


Fig. 8. Parameter identification on the SMO structure. (a)–(d) show the convergence process of the identified parameters k_1 , k_2 , H_0 , and θ_A^0 , respectively, and (e) shows the logarithm of δθ in each iteration step. The identified force-folding angle curve and the corresponding force-height curve of the SMO structure are displayed in (f) and (g), respectively, where the stable configurations are denoted by solid circles, and the unstable configuration by an empty circle.

Table 4Identification results of the SMO structure

Parameters	k ₁	k ₂	С	<i>X</i> ₀	θ_A^0
Identified values	0.0181 (N/rad)	2.1134 (N/rad)	1.0347 (kg/s)	0.0401 (m)	-0.5194 (rad)

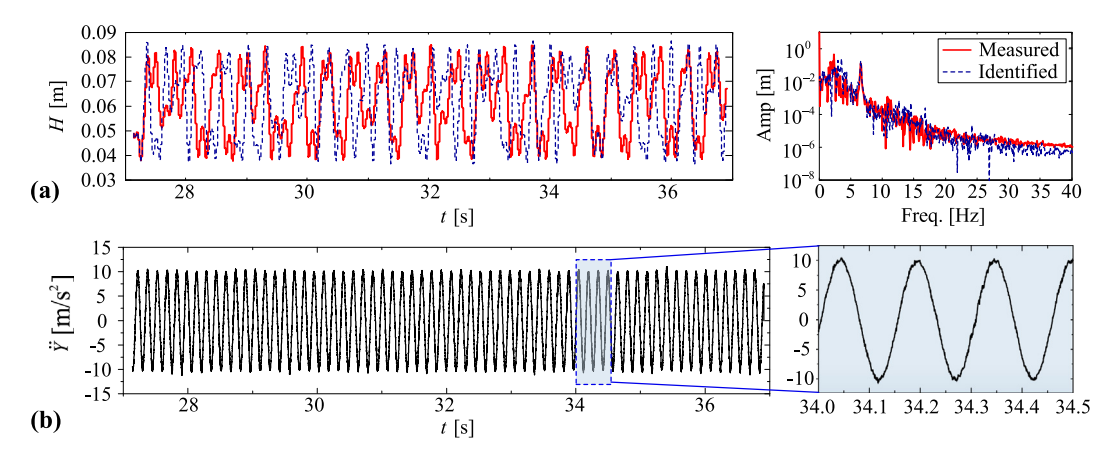


Fig. 9. (a) Comparison of the experimental and simulated response of SMO structure; (b) the noisy signal of excitation acceleration $\ddot{Y}(t)$.

in each step is presented in Fig. 8(a)–(d), and the overall error shows an exponential decrease (Fig. 8(e)). The identified values of the parameters are summarized in Table 4. It reveals that the identified value of k_2 is more than 110 times higher than k_1 , manifesting the fact that the crease stiffness k_2 originating from the spring-steel belts is much higher than the crease stiffness k_1 coming from the plastic film; the stress-free angle θ_A^0 locates within $(-\pi/2, \pi/2)$. With the identified parameters, the force-folding angle $(F_H - \theta_A)$ curve and the corresponding force-displacement $(F_H - H)$ curve are plotted in Fig. 8(f) and (g), respectively, which show obvious bistable characteristics, including two stable equilibrium (solid dots) and one unstable equilibrium (empty dot), as well as a segment with negative stiffness.

To verify the correctness of the identified results, we performed a simulation based on the identified parameters and applied the measured inputs. Since the exact initial conditions are unknown, the displacement and velocity at time zero (i.e., X(0) and $\dot{X}(0)$) are used as initial conditions instead. Fig. 9(a) shows the comparison between the measured and simulated response of X(t) - Y(t) in steady-state. Both responses exhibit obvious chaotic characteristics, manifesting as continuous spectrums over a limited range in their spectrogram, and they share very similar amplitudes. However, it is worth pointing out that the bistable SMO system is extremely sensitive to initial conditions, parameters, and input signals, especially for the chaotic responses. The measured initial conditions and input signals are corrupted by noise, which accounts for the quantitative differences between the measured and simulated responses. The noise effect is particularly non-negligible when we apply finite difference on the velocity single $\dot{Y}(t)$ to generate the excitation acceleration $\ddot{Y}(t)$ because the noise is amplified (Fig. 9(b)).

From another perspective, we verify the identification results via restoring force surface method [58], which reconstructs the force-displacement relationship from the measurements. In detail, based on the equation of motion (Eq. (46)) and Eq. (45), the restoring force and the height of the SMO structure at time instant t_i (i.e., $F_{H|_{t_i}}$ and $H|_{t_i}$) can be calculated from the measurements

$$F_{H}|_{t_{i}} = m\ddot{X}|_{t_{i}} + c \cdot (\dot{X}|_{t_{i}} - \dot{Y}|_{t_{i}}), \tag{50}$$

$$H|_{t_i} = X|_{t_i} - Y|_{t_i} + X_0, (51)$$

where $X|_{t_i}$ and $Y|_{t_i}$ are the measured displacement of the lumped mass and the base at time instant t_i , respectively; $\dot{X}|_{t_i}$ and $\dot{Y}|_{t_i}$ are the corresponding velocities; and $\ddot{X}|_{t_i}$ is the acceleration of the lumped mass, obtained by forward difference formula. Applying the above procedures at each measurement between 27 s and 37 s, a series of data $(H|_{t_i}, F_H|_{t_i})$ can be obtained, which are dotted on Fig. 10. The scatter diagram actually represents the restoring force acting on a mass at various positions and velocities. It has a good agreement with the identified force-displacement curve (solid), which again, manifests the correctness of the identification and the effectiveness of the proposed approach.

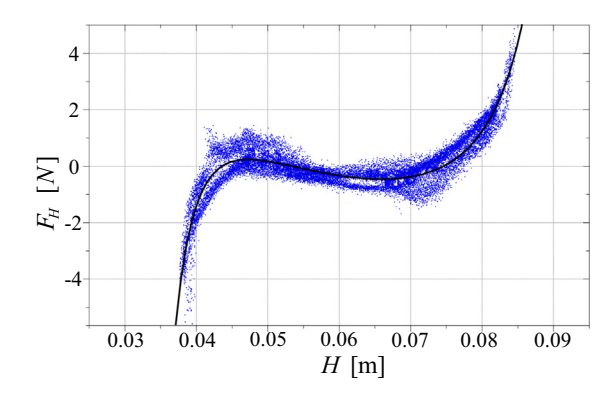


Fig. 10. Comparison between the identified force-displacement curve and the restoring force surface.

6. Conclusion

By applying the B-Spline Galerkin finite element method in time domain, this paper introduces a novel identification method for parameters in ordinary differential equations. Conventional identification techniques often require cumbersome numerical integration that is computationally inefficient, or discrete differences on data or analytical derivatives on basis functions that may unavoidably amplify the measurement noise. On the other hand, although still using B-Splines to globally construct the solutions, the proposed method eliminates the requirement of taking derivatives on basis function by employing the Galerkin weak formulation and integration by parts. Such procedures neither amplify the measurement noises nor impose high computation burden, therefore would exhibit broad applicability, high efficiency, and good robustness. These advantages are demonstrated through two intractable testbed problems: one is a high-dimensional coupled Chua's circuit that may exhibit chaotic responses and is sensitive to initial conditions and parameters; the other is the tank reactor equation, which is nonlinear in parameters and involves discontinuous input and output. Numerical simulations show that the proposed method could effectively and efficiently identify the parameters with high accuracy. Meanwhile, a bistable Miura-ori structure under base excitation is examined with the new method. Although the inherent bistability is a strong global nonlinearity, and the system exhibits complex dynamic behavior that is sensitive to initial conditions and parameters, the proposed method successfully identifies the geometrical and mechanical parameters and regenerates the constituent force-displacement relationship of the origami structure. Numerical simulations and the obtained restoring force surface demonstrate that the identification results agree well with the experiments.

It is worth noting at the end that there is no "one size fits all" approach for parameter identification. The proposed method does show advantages including numerical efficiency, noise robustness, and compatibility to complex nonlinearity and high dimensionality, but may still have challenges in certain scenarios and calls for additional improvements.

Acknowledgement

The authors would like to thank Dr. Suyi Li from the Clemson University and Ms. Huimin Ji from the University of Michigan for the kind assistance on experiments, and Dr. Xiaoxu Zhang from Tongji University for the helpful suggestions that were of great benefit to this work. This research was supported by the National Science Foundation of China under Awards No. 11572224 and No. 11772229, the U.S. National Science Foundation under Awards No. 1634545, and the University of Michigan Collegiate Professorship.

Appendix A. Geometry of the stacked Miura-ori (SMO) structure

Folding of the SMO structure is one degree-of-freedom, hence all the other dihedral angles between each two adjacent facets, i.e., $\rho_{xi}(x=A,B;i=1,2,3,4)$ and ρ_C can be expressed as functions of the folding angle θ_A and θ_B

$$\rho_{x1} = \rho_{x3} = \pi - 2\theta_x,
\sin \frac{\rho_{x2}}{2} = \frac{\cos \theta_x}{\sqrt{1 - \sin^2 \theta_x \sin^2 \gamma_x}},
\rho_{x4} = 2\pi - \rho_{x2}.$$
(A1)

For the bulged-out configuration ($\theta_A < 0$), we assign $\rho_{A2} \in (\pi, 2\pi)$; for the nested-in configuration ($\theta_A > 0$), $\rho_{A2} \in (0, \pi)$. The dihedral angles at the connecting creases are given as $\rho_C = \theta_B - \theta_A$.

References

- [1] D. Tall, The nature of mathematical proof 32 (1989) 28-32, https://doi.org/10.1007/s13398-014-0173-7.2.
- [2] S.L. Brunton, J.L. Proctor, J.N. Kutz, Discovering governing equations from data by sparse identification of nonlinear dynamical systems, Proc. Natl. Acad. Sci. 113 (2016) 3932–3937, https://doi.org/10.1073/pnas.1517384113.
- [3] Z. Li, M.R. Osborne, T. Prvan, Parameter estimation of ordinary differential equations, IMA J. Numer. Anal. 25 (2005) 264–285, https://doi.org/10.1093/imanum/drh016.
- [4] B.-N. Kim, S.W. Yoon, Nonlinear parameter estimation in water-saturated sandy sediment with difference frequency acoustic wave, Ultrasonics 49 (2009) 438–445, https://doi.org/10.1016/j.ultras.2008.11.002.
- [5] H. Xue, H. Miao, H. Wu, Sieve estimation of constant and time-varying coefficients in nonlinear ordinary differential equation models by considering both numerical error and measurement error, Ann. Stat. 38 (4) (2010) 2351.
- [6] J. Swartz, H. Bremermann, Discussion of parameter estimation in biological modelling: Algorithms for estimation and evaluation of the estimates, J. Math. Biol. 1 (1975) 241–257, https://doi.org/10.1007/BF01273746.
- [7] R. Bellman, J. Jacquez, R. Kalaba, S. Schwimmer, Quasilinearization and the estimation of chemical rate constants from raw kinetic data, Math. Biosci. 1 (1967) 71–76, https://doi.org/10.1016/0025-5564(67)90027-2.
- [8] H. Unbehauen, G.P. Rao, A review of identification in continuous-time systems, Annu. Rev. Control. 22 (1998) 145–171, https://doi.org/10.1016/S1367-5788(98)00015-7.
- [9] S.R. Anderson, V. Kadirkamanathan, Modelling and identification of non-linear deterministic systems in the delta-domain, Automatica 43 (2007) 1859–1868, https://doi.org/10.1016/j.automatica.2007.03.020.
- [10] B. Zhang, S.A. Billings, Identification of continuous-time nonlinear systems: The nonlinear difference equation with moving average noise (NDEMA) framework, Mech. Syst. Signal Process. 60 (2015) 810–835, https://doi.org/10.1016/j.ymssp.2015.01.009.
- [11] D. Coca, S. a. Billings, A direct approach to identification of nonlinear differential models from discrete data, Mech. Syst. Signal Process. 13 (1999) 739–755, https://doi.org/10.1006/mssp.1999.1230.
- [12] H. Howard Fan, T. Söderström, M. Mossberg, B. Carlsson, Y. Zou, Estimation of continuous-time AR process parameters from discrete-time data, IEEE Trans. Signal Process. 47 (1999) 1232–1244, https://doi.org/10.1109/78.757211.
- [13] T. Soderstrom, H. Fan, B. Carlsson, S. Bigi, Least squares parameter estimation of continuous-time ARX models from discrete-time data, IEEE Trans. Automat. Contr. 42 (1997) 659–673, https://doi.org/10.1109/9.580871.
- [14] T. Soderstrom, H. Fan, B. Carlsson, M. Mossberg, Some approaches on how to use the delta operator when identifying continuous-time processes, in: Proc. 36th IEEE Conf. Decis. Control, IEEE, San Diego, CA, 1997, pp. 890–895, https://doi.org/10.1109/CDC.1997.650755.
- [15] H. Garnier, L. Wang, Identification of Continuous-Time Models From Sampled Data, Springer London, London, 2008. 10.1007/978-1-84800-161-9.
- [16] K. Deng, L. Zhang, M.-K. Luo, A denoising algorithm for noisy chaotic signals based on the higher order threshold function in wavelet-packet, Chin. Phys. Lett. 28 (2011) 20502, https://doi.org/10.1088/0256-307X/28/2/020502.
- [17] J.D. Farmer, J.J. Sidorowich, Optimal Shadowing and Noise-reduction, Phys. D. 47 (1991) 373-392, https://doi.org/10.1016/0167-2789(91)90037-A.
- [18] J. Bröcker, U. Parlitz, M. OgorzaŁek, Nonlinear noise reduction, Proc. IEEE 90 (2002) 898–918, https://doi.org/10.1109/JPROC.2002.1015013.
- [19] L.A. Aguirre, S.A. Billings, Identification of models for chaotic systems from noisy data: implications for performance and nonlinear filtering, Phys. D Nonlinear Phenom. 85 (1995) 239–258, https://doi.org/10.1016/0167-2789(95)00116-L.
- [20] X.X. Zhang, J. Xu, Identification of time delay in nonlinear systems with delayed feedback control, J. Franklin Inst. 352 (2015) 2987–2998, https://doi. org/10.1016/j.jfranklin.2014.04.016.
- [21] S. Malik, G. Enzner, Fourier expansion of hammerstein models for nonlinear acoustic system identification, in: 2011 IEEE Int. Conf. Acoust. Speech Signal Process., IEEE, 2011: pp. 85–88. 10.1109/ICASSP.2011.5946334.
- [22] D. Brewer, M. Barenco, R. Callard, M. Hubank, J. Stark, Fitting ordinary differential equations to short time course data, Philos. Trans. R. Soc. A Math. Phys. Eng. Sci. 366 (2008) 519–544, https://doi.org/10.1098/rsta.2007.2108.
- [23] S. Wei, Q. Han, Z. Peng, F. Chu, Dynamic analysis of parametrically excited system under uncertainties and multi-frequency excitations, Mech. Syst. Signal Process. 72–73 (2016) 762–784, https://doi.org/10.1016/j.ymssp.2015.10.036.
- [24] C.M. Cheng, X.J. Dong, Z.K. Peng, W.M. Zhang, G. Meng, Wavelet basis expansion-based spatio-temporal Volterra kernels identification for nonlinear distributed parameter systems, Nonlinear Dyn. 78 (2014) 1179–1192, https://doi.org/10.1007/s11071-014-1506-y.
- [25] W.C. Su, C.Y. Liu, C.S. Huang, Identification of instantaneous modal parameter of time-varying systems via a wavelet-based approach and its application, Comput. Civ. Infrastruct. Eng. 29 (2014) 279–298, https://doi.org/10.1111/mice.12037.
- [26] B.W. Silverman, J.I.M. Ramsay, Functional Data Analysis, Springer-Verlag, New York, 2005. 10.1007/b98888.
- [27] H.L. Wei, S.A. Billings, J. Liu, Term and variable selection for non-linear system identification, Int. J. Control. 77 (2004) 86–110, https://doi.org/10.1080/00207170310001639640.
- [28] G.H. Golub, M. Heath, G. Wahba, Generalized cross-validation as a method for choosing a good ridge parameter, Technometrics 21 (1979) 215–223, https://doi.org/10.1080/00401706.1979.10489751.
- [29] K. Höllig, Finite element methods with B-splines, Society for Industrial and Applied Mathematics, Philadelphia, 2003. 10.1137/1.9780898717532.
- [30] S. Kutluay, A. Esen, I. Dag, Numerical solutions of the Burgers' equation by the least-squares quadratic B-spline finite element method, J. Comput. Appl. Math. 167 (2004) 21–33, https://doi.org/10.1016/j.cam.2003.09.043.
- [31] D. Pascual Serrano, C. Vera Pasamontes, R. Girón Moreno, Modelos animales de dolor neuropático, DOLOR 31 (2016) 70–76, https://doi.org/10.1017/ CB09781107415324.004.
- [32] T. Wang, Z. Wan, X. Wang, Y. Hu, A novel state space method for force identification based on the Galerkin weak formulation, Comput. Struct. 157 (2015) 132–141, https://doi.org/10.1016/j.compstruc.2015.05.015.
- [33] G.Q. Zhong, C.W. Wu, L.O. Chua, Torus-doubling bifurcations in four mutually coupled Chua's circuits, IEEE Trans. Circ. Syst. I Fundam. Theory Appl. 45 (1998) 186–193, https://doi.org/10.1109/81.661689.
- [34] T. Matsumoto, A chaotic attractor from Chua's circuit, IEEE Trans. Circ. Syst. 31 (1984) 1055-1058, https://doi.org/10.1109/TCS.1984.1085459.
- [35] L. Chua, M. Komuro, T. Matsumoto, The double scroll family, IEEE Trans. Circ. Syst. 33 (1986) 1072-1118, https://doi.org/10.1109/TCS.1986.1085869.
- [36] J.O. Ramsay, G. Hooker, D. Campbell, J. Cao, Parameter estimation for differential equations: a generalized smoothing approach, J. R. Stat. Soc. Ser. B Stat. Methodol. 69 (2007) 741–796, https://doi.org/10.1111/j.1467-9868.2007.00610.x.
- [37] S.B. Beale, Use of streamwise periodic boundary conditions for problems in heat and mass transfer, J. Heat Transf. 129 (2007) 601, https://doi.org/10.1115/1.2709976.
- [38] T. Pan, S. Li, W.-J. Cai, Lazy learning-based online identification and adaptive PID control: a case study for CSTR process, Ind. Eng. Chem. Res. 46 (2007) 472–480, https://doi.org/10.1021/ie0608713.
- [39] B.W. Bequette, W.B. Bequette, Process Dynamics; Modeling, Analysis, and Simulation, Prentice-Hall, New Jersey, 1998.
- [40] H. Fang, S. Li, H. Ji, K.W. Wang, Uncovering the deformation mechanisms of origami metamaterials by introducing generic degree-4 vertices, Phys. Rev. E. 94 (2016) 43002, https://doi.org/10.1103/PhysRevE.94.043002.
- [41] M. Schenk, S.D. Guest, Geometry of Miura-folded metamaterials, Proc. Natl. Acad. Sci. 110 (2013) 3276–3281, https://doi.org/10.1073/pnas.1217998110.
- [42] H. Yasuda, J. Yang, Reentrant origami-based metamaterials with negative Poisson's ratio and bistability, Phys. Rev. Lett. 114 (2015) 1–5, https://doi.org/10.1103/PhysRevLett. 114.185502.
- [43] H. Fang, S. Li, K.W. Wang, Self-locking degree-4 vertex origami structures, Proc. R. Soc. A Math. Phys. Eng. Sci. 472 (2016) 20160682, https://doi.org/10.1098/rspa.2016.0682.

- [44] S. Li, H. Fang, K.W. Wang, Recoverable and programmable collapse from folding pressurized origami cellular solids, Phys. Rev. Lett. 117 (2016) 114301, https://doi.org/10.1103/PhysRevLett. 117.114301.
- [45] S. Li, K.W. Wang, Fluidic origami with embedded pressure dependent multi-stability: a plant inspired innovation, J. R. Soc. Interface. 12 (2015) 20150639.
- [46] J.L. Silverberg, J. Na, A.A. Evans, B. Liu, T.C. Hull, C.D. Santangelo, et al, Origami structures with a critical transition to bistability arising from hidden degrees of freedom. Nat. Mater. 14 (2015) 389–393. https://doi.org/10.1038/NMAT4232.
- [47] S. Waitukaitis, R. Menaut, B.G. Chen, M. van Hecke, Origami multistability: from single vertices to metasheets, Phys. Rev. Lett. 114 (2015) 55503, https://doi.org/10.1103/PhysRevLett. 114.055503.
- [48] H. Yasuda, C. Chong, E.G. Charalampidis, P.G. Kevrekidis, J. Yang, Formation of rarefaction waves in origami-based metamaterials, Phys. Rev. E. 93 (2016) 43004, https://doi.org/10.1103/PhysRevE.93.043004.
- [49] S. Babaee, J.T.B. Overvelde, E.R. Chen, V. Tournat, K. Bertoldi, Reconfigurable origami-inspired acoustic waveguides, Sci. Adv. 2 (2016), https://doi.org/10.1126/sciadv.1601019, e1601019-e1601019.
- [50] H. Fang, S. Li, H. Ji, K.W. Wang, Dynamics of a bistable Miura-origami structure, Phys. Rev. E. 95 (2017) 52211, https://doi.org/10.1103/ PhysRevE.95.052211.
- [51] S. Lenci, G. Rega, Forced harmonic vibration in a duffing oscillator with negative linear stiffness and linear viscous damping, in: I. Kovacic, M.J. Brennan (Eds.), Duffing Equ. Nonlinear Oscil. Their Behav., first ed., John Wiley & Sons, 2011: pp. 219–276. 10.1002/9780470977859 (ch7).
- [52] H. Fang, K.W. Wang, Piezoelectric vibration-driven locomotion systems Exploiting resonance and bistable dynamics, J. Sound Vib. 391 (2017) 153–169, https://doi.org/10.1016/j.jsv.2016.12.009.
- [53] Z. Wu, R.L. Harne, K.-W. Wang, Excitation-induced stability in a bistable duffing oscillator: analysis and experiments, J. Comput. Nonlinear Dyn. 10 (2014) 1–26, https://doi.org/10.1115/1.4026974.
- [54] R.L. Harne, K.W. Wang, Harnessing Bistable Structural Dynamics for Vibration Control, Energy Harvesting, and Sensing, John Wiley and Sons, 2017.
- [55] B. Qiao, X. Zhang, X. Luo, X. Chen, A force identification method using cubic B-spline scaling functions, J. Sound Vib. 337 (2015) 28–44, https://doi.org/10.1016/j.jsv.2014.09.038.
- [56] X. Zhang, R.X. Gao, R. Yan, X. Chen, C. Sun, Z. Yang, Multivariable wavelet finite element-based vibration model for quantitative crack identification by using particle swarm optimization, J. Sound Vib. 375 (2016) 200–216, https://doi.org/10.1016/j.jsv.2016.04.018.
- [57] J. R., C. de Boor, A Practical Guide to Splines., Math. Comput. 34 (1980) 325. 10.2307/2006241.
- [58] S.F. Masri, T.K. Caughey, A nonparametric identification technique for nonlinear dynamic problems, J. Appl. Mech. 46 (1979) 433, https://doi.org/10.1115/1.3424568.